Analyzing the orientation dependence of stresses in polycrystals using vertices of the single crystal yield surface and crystallographic fibers of orientation space

Hadas Ritz *, Paul Dawson, Tito Marin

196 Rhodes Hall, Cornell University, Ithaca, NY 14853, USA

ARTICLE INFO

ABSTRACT

The influence of the polygonal geometry of the restricted slip-associated yield surface on the distribution of stresses over a polycrystalline aggregate is examined. The vertices of the yield surface (stress states corresponding to polyslip) are grouped according to symmetries imposed by crystal structure. A measure of coaxiality between crystal stresses and yield surface vertex stresses is used to quantify the proximity of the stress in each crystal to a yield surface vertex. It is shown that for prescribed stress states, crystal stresses align more closely with certain families of vertices than with others and this relation between crystal and vertex stresses is found to depend on crystallographic fibers. Using this information, the stress distributions from finite element simulations of face centered cubic polycrystals are analyzed for different stress states ranging from uniaxial to balanced biaxial. Over the fundamental region of orientations, the propensity for the stress to align with a vertex is demonstrated. Further, the stresses in elements contributing to certain crystallographic fibers are shown to favor the vertex families aligned with those fibers. The implications of these results on mechanical behaviors, especially with respect to those observed in diffraction experiments, are discussed.

1. Introduction

Quantifying stress distributions in polycrystalline solids is critical to better assessing a material's performance under load. Stress is the driving force for structural degradation associated with the processes that lead to damage and failure. Plastic flow within crystals usually precedes and accompanies the structural degradation and contributes strongly to it. From years of experience with engineering alloys, it is known that plastic flow and structural changes associated with it are closely linked to the underlying structure of the constituent crystals. Of course, it is also true that these behaviors are strongly dependent on the stress acting on those crystals. Quantifying the stress distribution within a loaded polycrystal is not a simple task, however, as it requires understanding both the properties of individual crystals and their collective behavior as an aggregate. To evaluate the collective behavior, we must accommodate the fact that a polycrystalline solid under load is a statically indeterminate body with the stress distribution and deformation field together satisfying equilibrium, compatibility, and the material's constitutive behavior. Because the properties of individual crystals are anisotropic and their lattice orientations do not coincide, the stress is heterogeneous at the crystal scale even if the loading mode is simple at the macroscopic scale. Consequently, to better understand deformation and failure in polycrystalline solids, considerable attention has been given to quantifying the heterogeneity of stress and strain within and among

---

* Corresponding author. Tel.: +1 607 255 5695; fax: +1 607 255 1222.
E-mail addresses: hr32@cornell.edu (H. Ritz), prd5@cornell.edu (P. Dawson), marin@ied.eng.unipr.it (T. Marin).

crystals. Experimentally, total strain distributions have been mapped by various microscopy and digital image correlation methods (Chu et al., 1985; Efstathiou et al., 2008). Elastic strains have been measured by X-ray and neutron diffraction using the lattice distortions detected by shifts in the Bragg peaks under *in situ* loading in samples taken into the elastic–plastic regime (MacEwen et al., 1983; Clausen and Lorentzen, 1997; Holden et al., 1997; Miller et al., 2005; Marin et al., 2008). As it is the elastic strains that are proportional to stress through Hooke's law, these measurements offer direct evidence of the stress state. Many of the diffraction measurements were taken over diffraction volumes that were large with respect to individual grains of the sample and thus incorporate the heterogeneity of stress inherent in deforming polycrysts (Pang et al., 1998; Daymond et al., 2005; Bernier and Miller, 2006).

Numerical simulation of deforming polycrystals also provides a valuable tool for quantifying stress distributions at the crystal scale. For examining issues related to the spatial heterogeneity of stress, finite element formulations of crystal-scale elastoplasticity have demonstrated considerable utility (Needleman et al., 1985; Kalidindi et al., 1992; Dawson and Marin, 1998). Over the past 20 years, many studies have focused on texture evolution over large strains, plastic strain distributions, and phase transformations, as exemplified by Mathur and Dawson (1989), Raabe et al. (2001), Barton et al. (2005), Maniatty et al. (2008). Of special interest here are a number of the studies that include direct comparisons of elastic strains obtained by finite element simulation with values measured via *in situ* diffraction (Dawson et al., 2000; Hartig and Mecking, 2005; Miller et al., 2008). Finite element simulations render approximate solutions to the governing equations for a set of applied boundary and initial conditions. These solutions exhibit spatial fluctuations consistent with the level of structural heterogeneity of the polycrystal. When examining the stress distributions, one easily observes these spatial fluctuations, but discerning patterns or correlations with the crystal lattice orientations often is very difficult. Yet, if we turn to the properties peculiar to crystals undergoing plastic deformation by slip, we can extract from these distributions definite trends between the stress and the lattice orientations of the crystals. The key is the strong constraint that restricted slip plays to define the orientation dependence of the crystal stresses during plastic flow. Exploiting the attributes of this constraint to better understand stress distributions in polycrystals, and their particular relation to diffraction data, is the focus of this paper.

Restricted slip in crystalline solids refers to the tendency crystals exhibit to deform by means of slip on close-packed planes in close-packed directions (Honeycombe, 1984). From the kinetics of dislocation motion that facilitates slip, slip is an inelastic, rate-dependent process, expressed as the slip rate being a nonlinear function of the resolved shear stress (expressed mathematically in Section 3.2.) The slip systems for a given type of crystal are defined by the available combinations of slip planes and slip directions, which together with the kinetic equations for slip define the crystal's anisotropic yield surface in stress space. Within a reference frame tied to the crystal lattice, the topological features of a yield surface have fixed orientation at fixed mechanical state (but possibly change with strain hardening). Thus, the orientation of the yield surface for a particular crystal sitting in an aggregate of crystals depends on the orientation of the crystal's lattice. In many formulations with the capability to accommodate spatial variability of deformation over a polycrystal (including finite element formulations), the equations for rate dependent slip define the plastic response while Hooke's law is taken for the elastic behavior. These elastic and plastic behaviors both are anisotropic, but do not display the same dependency on orientation of the crystallographic lattice. As a consequence, the stress state over a polycrystal redistributes as the stress intensifies from levels within the elastic domain to ones that induce plastic flow where the equations of slip, or equivalently the single crystal yield surfaces, actively constrain the stress state.

Crystals that share some commonality with respect to lattice orientation might be expected to share related commonality with respect to features of the yield surface. This is true for crystals lying on a crystallographic fiber: a line in orientation space along which lattice orientations differ only by rotation about one crystallographic direction. For crystals along a fiber, the yield surfaces appear rotated with respect to each other. Depending on the fiber and the applied stress, this has strong implications on whether that collection of crystals will all experience the same stress and to what extent their stresses will deviate from the nominal value. Crystallographic fibers are intimately related to diffraction measurements, as the orientations of those crystals that satisfy a particular Bragg condition and collectively contribute to an individual strain measurement lie on a common fiber. This motivates the effort to explore the influence of fiber-related orientation dependence of the crystal yield surface on the distributions of crystal stress.

In this paper we examine the stress distribution in aggregates of face-centered cubic (fcc) crystals for nominal stress states varying from uniaxial tension to balanced biaxial tension. The constitutive behavior is specified at the crystal level: anisotropic elasticity for cubic symmetry and plasticity by rate dependent slip on a restricted number of systems. The stress distributions are computed for virtual aggregates using a finite element formulation and show clear dependencies on crystal orientation. We begin in Section 2 by reviewing some basic definitions for orientations of crystals and relations associated with crystallographic fibers. Turning next to the crystal yield surface, in Section 3 we examine its rate-independent limit as an aid in interpreting the stress values computed with the rate dependent model. We first review the yield surface topology including its vertices defined by stresses that can activate multiple slip systems simultaneously. We show that the vertex stresses fall into one of five families of vertices. For specified applied stresses at the crystal scale, one or two families are favored over the others for crystals aligned with a particular fiber. Our methodology for the simulations and analysis is presented in Section 4. Our results are presented in Sections 5 and 6 demonstrating that the computed crystal stresses for crystals associated with common fibers tend to align with the more favorable yield surface vertex families for the fiber. From these, we show that the stress distribution over the polycrystal follows in part from the structure suggested by the fibers. As discussed in Section 7, this gives insight not only for the interpretation of diffraction

data specifically, but also more generally into the relative influences of neighborhood and orientation and into the manner in which crystal stresses deviate from the nominal stress during plastic flow.

2. Orientations of the crystal lattice

The orientation dependence of the mechanical properties of polycrystalline materials follows from the crystal (lattice) structure of the constituent grains and the distribution of lattice orientations. Thus we begin by introducing a parameterization for orientation. The relationship that defines a crystallographic fiber is then presented along with a convention for identifying specific fibers.

2.1. Orientations of individual crystals

Each grain within an aggregate has a set of local orthonormal coordinate axes, (C_1, C_2, C_3), tied to its crystal lattice. Any direction or plane within a grain is defined with respect to these axes. The orientation of the crystal lattice is related to a reference coordinate system of the specimen or laboratory, (S_1, S_2, S_3), using an angle-axis parameterization (Altmann, 1986; Becker and Panchanadeeswaran, 1989; Morawiec and Pospiech, 1989). We employ the parameterization due to Rodrigues:

$$\boldsymbol{r} = \boldsymbol{n}\tan\frac{\beta}{2}, \tag{1}$$

where the Rodrigues vector, $\boldsymbol{r}$, is calculated from the axis of rotation, $\boldsymbol{n}$ (expressed in terms of the S_i) and the angle of rotation about that axis, β. It is important to note that the cubic crystals considered here have a high degree of symmetry and therefore a subset of orientation space, known as the fundamental region, should be used. A fundamental region is the subset of all orientations that includes all symmetrically unique possible orientations given a certain crystal symmetry. To aid in the description of crystallographic fibers, we introduce an orientation tensor that also defines a grain's crystallographic orientation, $\mathbf{R}$, as taking a vector in crystal coordinates, $\boldsymbol{v^c}$, into the sample framework, $\boldsymbol{v^s}$:

$$\mathbf{R}\boldsymbol{v^c} = \boldsymbol{v^s}. \tag{2}$$

The rotation tensor is obtained directly from the Rodrigues vector as

$$\mathbf{R} = \frac{1}{1 + \boldsymbol{r} \cdot \boldsymbol{r}}(\mathbf{I}(1 - \boldsymbol{r} \cdot \boldsymbol{r}) + 2(\boldsymbol{r} \otimes \boldsymbol{r} + \mathbf{I} \times \boldsymbol{r})), \tag{3}$$

where $\mathbf{I}$ is the identity tensor.

In addition to considering the orientation of each crystal individually within a polycrystal, it is also possible to examine the set of all orientations represented therein. The orientation distribution function (ODF) is a function, $A(\boldsymbol{r})$, that indicates the relative frequency with which each possible orientation occurs in the bulk. In a polycrystal for which each orientation occurs with equal frequency or likelihood $A(\boldsymbol{r})$ is constant over the fundamental region. This is referred to as uniform texture and is the main situation considered in this paper.

2.2. Crystallographic fibers

Frequently, it is instructive to examine the collective behavior of subsets of the crystals comprising a polycrystal. Subsets defined by a common orientational condition are of special interest because of the connections between the lattice structure and the crystal properties. An example is the directional Young's modulus, which relates uniaxial stress in a crystal direction to normal lattice strain in that direction, and depends only on the orientation of that direction within the crystal, not on the complete crystal orientation. A typical diffraction measurement shows information from all crystals having a particular crystal axis, $\boldsymbol{c}$, aligned with the scattering vector, $\boldsymbol{s}$. This includes all crystals with their orientation, $\mathbf{R}$, satisfying

$$\mathbf{R}\boldsymbol{c} = \pm\boldsymbol{s}. \tag{4}$$

The collection of crystals satisfying that equation is the fiber of $\boldsymbol{c} \| \boldsymbol{s}$ and can be represented by $\mathbf{R}_{[\boldsymbol{c}][\boldsymbol{s}]}$. In the uniaxial simulations presented later in this paper the tension direction is along the z-axis and much of the analysis focusses on the axial scattering vector. For simplicity's sake, therefore, "the hkl fiber" refers to $\mathbf{R}_{[h\,k\,l][0\,0\,1]}$ unless otherwise specified. Several of the fibers considered in this study are shown through the Rodrigues space cubic fundamental region in Fig. 1. When plotted in Rodrigues space, all crystallographic fibers appear as straight lines (Kumar and Dawson, 2000). If only the fundamental region of Rodrigues space is considered, each fiber may appear as several straight line segments, emerging from and reentering the fundamental region several times. This attribute of representing crystallographic fibers as straight line segments makes Rodrigues space an ideal choice for visualizing fiber-dependent crystal properties throughout orientation space, and we therefore utilize it here.

Crystallographic fibers are of interest experimentally not only because they typically represent the crystals from which diffraction measurements are taken, but also because taking averages of values along fibers is necessary for pole figure
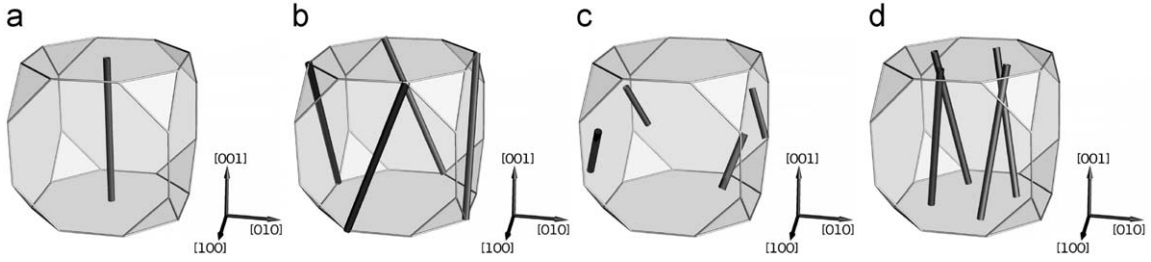
Fig. 1. Several fibers shown in the cubic fundamental region of Rodrigues space. All of these fibers have a crystal axis parallel to the [0 0 1] sample direction. (a) $\mathbf{R}_{[1\,0\,0]|[0\,0\,1]}$. (b) $\mathbf{R}_{[1\,1\,0]|[0\,0\,1]}$. (c) $\mathbf{R}_{[1\,1\,1]|[0\,0\,1]}$. (d) $\mathbf{R}_{[3\,1\,1]|[0\,0\,1]}$.

construction. For example, to construct a lattice strain pole figure, for one choice of $\boldsymbol{c}$ the $\mathbf{R}_{[\boldsymbol{c}]|[\boldsymbol{s}]}$ fiber is found for many sample directions. Each component of lattice strain can then be averaged among all of the crystals which lie along each fiber, giving the value of that component of lattice strain on the $\boldsymbol{c}$ lattice strain pole figure. Similarly, pole density figures may be constructed by finding the number of crystals contributing to $\mathbf{R}_{[\boldsymbol{c}]|[\boldsymbol{s}]}$ for one choice of $\boldsymbol{c}$ and all possible values of $\boldsymbol{s}$, or inverse pole figures by choosing one $\boldsymbol{s}$ and all possible $\boldsymbol{c}$.

3. Crystal stresses and the single crystal yield surface

A framework of comparison between different stress states is necessary in understanding stress distributions within polycrystals. That framework is provided here, including both a convention for representing stress and a measure of similarity between stress states. Furthermore, since we assume that as crystals move through elastic to plastic deformation their behavior is dictated by the single crystal yield surface, we present our usage of that yield surface.

3.1. Representing the stress and its relative direction

All stress states considered are three-dimensional Cauchy stress tensors, $\boldsymbol{\sigma}$. The deviatoric portion of the stress, $\boldsymbol{\sigma}'$, is often of interest. It is the non-volumetric portion of the stress, and, as will be discussed in detail in the following section, it is the driving force behind plastic deformation. The deviatoric stress is calculated as

$$\boldsymbol{\sigma}' = \boldsymbol{\sigma} + \pi\mathbf{I}, \tag{5}$$

where $\pi \equiv -\frac{1}{3}\mathrm{tr}\,\boldsymbol{\sigma}$ is the pressure. Note that $\boldsymbol{\sigma}$ has six independent components while $\boldsymbol{\sigma}'$ is five dimensional. The pressure is the remaining independent degree of freedom.

Owing to the anisotropy of single crystals, the orientation of a grain relative to the loading is critical to the behavior it exhibits. More particularly, which directions in the crystal lattice are oriented parallel to the principal axes of the applied load tell us a great deal about how the crystal will respond to that load. Since the deviatoric stress can be considered to consist of a magnitude and a direction in the deviatoric stress space, it is simple to use a dot product to understand the relationship between stress states. The coaxiality, ϕ_a^b, between $\boldsymbol{\sigma}_a'$ and $\boldsymbol{\sigma}_b'$ is calculated as

$$\phi_a^b = \cos^{-1}\left(\frac{\boldsymbol{\sigma}_a' : \boldsymbol{\sigma}_b'}{\|\boldsymbol{\sigma}_a'\|\|\boldsymbol{\sigma}_b'\|}\right). \tag{6}$$

If $\boldsymbol{\sigma}_a'$ and $\boldsymbol{\sigma}_b'$ have the same direction in deviatoric stress space then ϕ_a^b, which is the angle between the two vectors, will be 0. The smaller the magnitude of ϕ_a^b, the more closely aligned are the two stress states being compared. In general ϕ_a^b will have a maximum value of 180° which occurs when the stresses point in opposite directions in deviatoric stress space. Note that $\phi_a^b = \phi_b^a$ and the two may be used interchangeably. Throughout this paper "a" and "b" may take the value of "m" to represent applied or macroscopic stress, "c" to represent crystal stress, and "v" to represent a yield surface vertex stress.

3.2. Single crystal yield surfaces (SCYS)

Yield surfaces dictate if and how a material may plastically deform. We consider the case of face centered cubic (fcc) crystals deforming via slip on {1 1 1} planes in $\langle 1\,\bar{1}\,0 \rangle$ directions (Honeycombe, 1984; Hosford, 1993). Slip occurs if the resolved shear stress, τ^α, on a slip system α is equal to the critical resolved shear stress, g^α, on that system, as in

$$\tau^\alpha \equiv (\boldsymbol{b}^\alpha \otimes \boldsymbol{m}^\alpha) : \boldsymbol{\sigma} = g^\alpha, \tag{7}$$

where $\boldsymbol{b}^\alpha$ and $\boldsymbol{m}^\alpha$ are the slip direction and slip plane normal for the α slip system, respectively, and $\boldsymbol{\sigma}$ is the stress state in the crystal (Kocks et al., 1998).

In the rate dependent case, g^α is a function of temperature and strain rate; in the rate independent case it is not (Klepaczko and Chiem, 1986; Kocks et al., 1998). Rate independent behavior is the limit for vanishing strain rate sensitivity. Given the low rate sensitivity of the metals of interest, the rate independent limit provides an excellent construct for

examining the orientation dependence of the active stress in a crystal even though the stress is being computed with a rate dependent model.

The rate-independent single crystal yield surface is a polytope in five-dimensional (deviatoric) space formed by the inner envelope of the set of planes defined by Eq. (7) for all slip systems (Kocks, 1970). If the stress in a crystal lies on a face of the yield surface, the crystal is plastically deforming via slip on the slip system forming that face. In geometric terms, a facet of the yield surface corresponds to the plane defined by the stress condition necessary to activate one slip system. When the stress in a crystal is on the SCYS, the plastic strain increment is always normal to the SCYS in the slip-based model employed here (Canova et al., 1985; Phillips and Sierakowski, 1965).

More than one slip system can be activated if the crystal stress lies at the intersection of two or more planes so that conditions for slip are satisfied for multiple slip systems. The shape of the SCYS thus includes facets where one slip system is yielding, edges defined by between two and four slip systems yielding, and vertices where at least five slip systems are yielding and "polyslip" may be said to occur (Kocks, 1960). For the case we consider here there are 24 facets corresponding to the positive and negative stresses on the 12 fcc slip systems and 56 vertices in the SCYS in deviatoric stress space. A portion of a simplified two-dimensional schematic of a SCYS is shown in Fig. 2. It shows two crystals' stresses: one within the elastic regime and not reaching the SCYS facet, and one in the plastic regime, touching the SCYS. The coaxiality between the plastically deforming crystal stress and the nearest vertex is labeled in the figure as well.

Polyslip is a condition that can accommodate arbitrary deviatoric strain. In a polycrystal, compatibility constrains the crystals from deforming independently of each other. Instead of being able to activate only the single most favorably oriented system, crystals are forced into modes that activate multiple slip systems, or polyslip. Since crystal stresses can never exceed the bounds of the yield surface, if a crystal is within an aggregate that is subjected to an increasing external stress, its stress will rise, driven primarily by the applied external loading (though highly influenced by the elastic anisotropy and neighboring grains), until it reaches a facet of the SCYS. Once the stress lies on the SCYS, plastic straining can accompany the elastic straining. Of the total strain increment, only the plastic portion is constrained to be in a direction normal to the SCYS. The elastic portion of the strain increment may have a part that is parallel to the SCYS, which in general indicates a direction change for the stress. This change moves the stress towards another facet of the SCYS and eventually into a vertex (called a vertex stress) to accommodate any arbitrary direction of macroscopic stress. This implies that after a sufficient amount of plastic strain in a bulk material, it is likely that the deviatoric stresses within each crystal will correlate well with vertices on the SCYS (Kocks et al., 1983; Maniatty and Yu, 1996; Barton et al., 1999), and not necessarily with the externally applied stress. In this way the stresses within individual crystals in a polycrystal can accommodate the compatibility constraint. Which of the many vertex stresses a crystal chooses depends in part on its neighborhood, as equilibrium must be maintained over the polycrystal.

In cases of polyslip where more than five independent slip systems may be activated, the issue of redundancy must be resolved; that is, what are the relative shearing rates of the potentially active slip systems in cases where there are many (perhaps infinitely many) combinations that produce the same net deformation. This issue has been examined in detail for rate independent models by a number of researchers (Arminjon, 1991; Franciosi and Berbenni, 2007). It has also been circumvented by allowing highly spatially heterogeneous deformation modes involving regions of single slip within single crystals (Conti and Ortiz, 2005; Conti et al., 2007). This is not an issue here as we use the rate independent SCYS only to understand the orientation dependence of the crystal stresses, having actually computed the crystal stresses using a rate-insensitive model that uniquely determines the slip system activities while retaining much of the geometric character of the rate independent polytope surface. The influence of the rate sensitivity on the results is reported in a number of studies (Beausir et al., 2007; Maniatty and Yu, 1996; Maniatty et al., 2008; Busso and Cailletaud, 2005; Knockaert et al., 2000; Graff et al., 2007). Provided that the rate sensitivity is relatively low (rate insensitive behavior), the trends regarding polyslip remain qualitatively similar in regards to features of the SCYS.

Strain hardening has the effect of expanding the SCYS. If all slip systems harden identically, the topology of the SCYS remains unchanged. There are alternative models of slip system hardening which allow the slip systems to harden at different rates (see for example Holmedal et al., 2008; Zhao et al., 2008; Cuitino and Ortiz, 1992; Zhang et al., 2009; Bridier et al., 2009), in which case the topology may change with continued straining. However, even in such cases the current
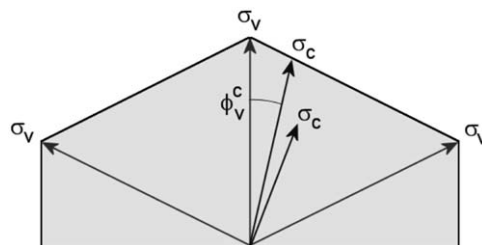

Fig. 2. A two-dimensional schematic of a SCYS showing several vertex stresses, two crystal stresses, and the coaxiality between one crystal stress and one vertex stress. The sharp vertices shown in this figure are indicative of a rate independent yield surface. In the rate dependent case the vertices would be slightly rounded corners.

H. Ritz et al. / J. Mech. Phys. Solids 58 (2010) 54–72

59

yield surface will retain a polytope character and polyslip will be associated with crystal stresses aligned with a vertex stress (Mecking et al., 1996). The same can be said for situations with unequal slip system strengths as an initial condition. Our analysis method can be applied to any polytopic yield surface for which vertex stresses can be identified.

The movement of crystal stress from a yield surface facet towards a vertex stress should not be confused with a physical reorientation of the crystal lattice. Crystal stresses align with vertex stresses very early in the plastic deformation (1% strain or less), whereas the amount of mechanical strain necessary before significant crystal lattice reorientation occurs is typically much higher (Kumar and Dawson, 2009; Miehe and Rosato, 2007). Since the relative time necessary for the crystal stresses to align with the vertex stress is low, even as the crystal does experience hardening or reorientation the stress is able to track the movement of the vertex.

3.3. Vertex families

The positive and negative vertices are treated simultaneously, thereby limiting further analysis to consider 28 vertices. These 28 positive vertices in the SCYS represent five distinct stress states which produce distinct types of polyslip. Bishop (1953) and Kocks et al. (1983) report these polyslip types as [1 0 0] tension, [1 1 1] tension, (1 0 0)[0 1 0] shear, [1 0 0] compression with (1 0 0)[0 1 1] shear, and (1 0 0)[0 1 0] shear with (1 1 0)[1 1 0] shear. For each of these types a unique vertex, $\mathbf{v}$, can be found by taking the symmetric part of the outer product of the plane normal, $\boldsymbol{n}$, and the traction, $\boldsymbol{t}$, and then finding the deviatoric portion of that stress:

$$\boldsymbol{\sigma} = \mathrm{sym}(\boldsymbol{n} \otimes \boldsymbol{t}), \quad \mathbf{v} = \boldsymbol{\sigma}'. \tag{8}$$

Vertex families 4 and 5 must be generated by applying the first part of Eq. (8) to both of the mentioned $(\boldsymbol{n}, \boldsymbol{t})$ pairs and summing those results before taking the deviatoric portion. For example, the second family of vertices can be generated by finding the deviatoric stress state due to any of the following $(\boldsymbol{n}, \boldsymbol{t})$ pairs: $((1\,1\,1),[1\,1\,1])$, $((\overline{1}\,1\,1),[\overline{1}\,1\,1])$, $((1\,\overline{1}\,1),[1\,\overline{1}\,1])$, $((1\,1\,\overline{1}),[1\,1\,\overline{1}])$, $((\overline{1}\,\overline{1}\,1),[\overline{1}\,\overline{1}\,1])$, $((1\,\overline{1}\,\overline{1}),[1\,\overline{1}\,\overline{1}])$, $((\overline{1}\,1\,\overline{1}),[\overline{1}\,1\,\overline{1}])$, $((\overline{1}\,\overline{1}\,\overline{1}),[\overline{1}\,\overline{1}\,\overline{1}])$. Applying Eq. (8) to each of those pairs results in only four unique vertex stress states since, for example, both $((1\,1\,1),[1\,1\,1])$ and $((\overline{1}\,\overline{1}\,\overline{1}),[\overline{1}\,\overline{1}\,\overline{1}])$ generate

$$\mathbf{v} = \begin{bmatrix} 0 & 1 & 1 \\ 1 & 0 & 1 \\ 1 & 1 & 0 \end{bmatrix}.$$

The stress states in family 2 have all zero normal stresses and all shear stresses of equal magnitude, with at most one negative shear. However, these four seemingly unique stress states are in fact indistinguishable from each other when the crystal symmetry is taken into account. Although in finite element simulations it is possible to define a particular orientation for an element or grain and therefore to differentiate between a stress state close to one of these vertices versus another, in an actual material it is impossible to distinguish between symmetrically equivalent orientations, and therefore impossible to distinguish between these four vertex stresses. The same can be said of the other four vertex families. When performing comparisons between vertex stresses and macroscopic or crystal stresses via Eq. (6) it is necessary to use only one member of each vertex family along with all symmetry operators for cubic crystals, $\mathbf{R}^{\mathrm{sym}}$.

3.4. Coaxiality between vertex stress and applied stress

Fig. 3 demonstrates the existence of the SCYS vertex families. It shows $\phi_{\mathrm{v}}^{\mathrm{m}}$ calculated from Eq. (6) using $\boldsymbol{\sigma}_{\mathrm{v}}'$ for each of the 28 positive vertices and $\boldsymbol{\sigma}_{\mathrm{m}}'$ for an ideal applied uniaxial tension in the z-direction (i.e. $\sigma_{zz} = 1$ and all other $\sigma_{ij} = 0$) for single crystals on several fibers $\mathbf{R}_{\{\boldsymbol{c}\}[0\,0\,1]}$. For each fiber the crystal orientation has been taken into account in addition to crystal symmetries, $\mathbf{R}^{\mathrm{sym}}$, since the vertex stress states are relative to the crystal axes. The angle of coaxiality between the vertices and the given applied macroscopic stress state falls into five discrete values for each fiber. Vertices numbered 1–3 comprise the first family, numbers 4–7 comprise the second family, and so on.[1] These families, numbered along the top of Fig. 3, correspond to types A–E of polyslip from Kocks (1960).

For this particular set of fibers and applied loading conditions, any single crystal whose orientation belongs to a single crystallographic fiber will generate the same degree of coaxiality between a vertex and the applied stress. This is because the applied stress is isotropic in the plane perpendicular to $\boldsymbol{s}$ used to calculate the fiber. Details of that condition are presented in Appendix A. Only a single representative orientation is needed to calculate the vertex coaxialities to the applied stress for each fiber, and $\phi_{\mathrm{v}}^{\mathrm{m}}$ is calculated using $\boldsymbol{\sigma}_{\mathrm{v}} = \mathbf{R}\mathbf{v}\mathbf{R}^{T}$ $\forall \mathbf{R} \in \mathbf{R}^{\mathrm{sym}}$. The minimum value over all symmetries is saved as the coaxiality between that vertex and the applied stress for that fiber.

If a change is made in either the applied stress, $\boldsymbol{\sigma}_{\mathrm{m}}'$, or the sample direction used to calculate the fiber, $\boldsymbol{s}$, the situation becomes more complicated. The coaxiality between the vertex stress and the applied stress is no longer constant for any crystal orientation along the fiber. Fig. 4 shows $\phi_{\mathrm{v}}^{\mathrm{m}}$ for each of the five vertex families for $\mathbf{R}_{\{1\,1\,1\}[0\,0\,1]}$ for four different applied stress states, representing levels of biaxiality ranging from uniaxial tension in the z-direction to balanced biaxiality

---

[1] The vertex numbers are arbitrary, but those individual vertices belonging to the same vertex family have purposely been numbered consecutively for graphical clarity.
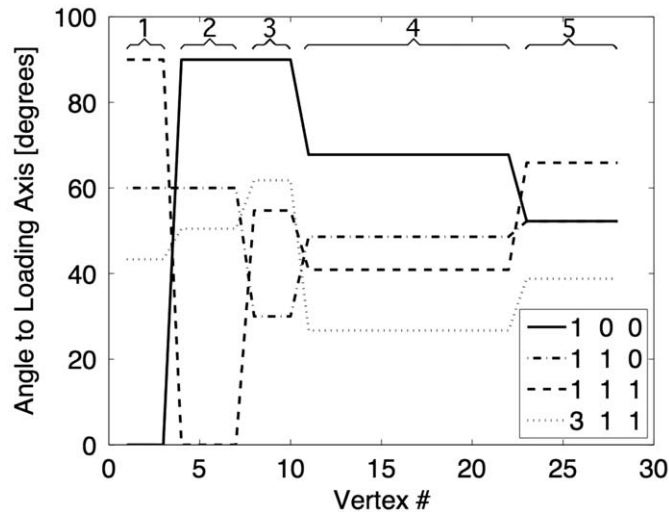
Fig. 3. For several fibers $\mathbf{R}_{\{c\}|[0\,0\,1]}$, the coaxiality ϕ_v^m is shown for each of the vertices and a macroscopic stress state of uniaxial tension along the z-axis. Five vertex families, each composed of a set of symmetrically equivalent SCYS vertices, are labeled at the top of the figure.
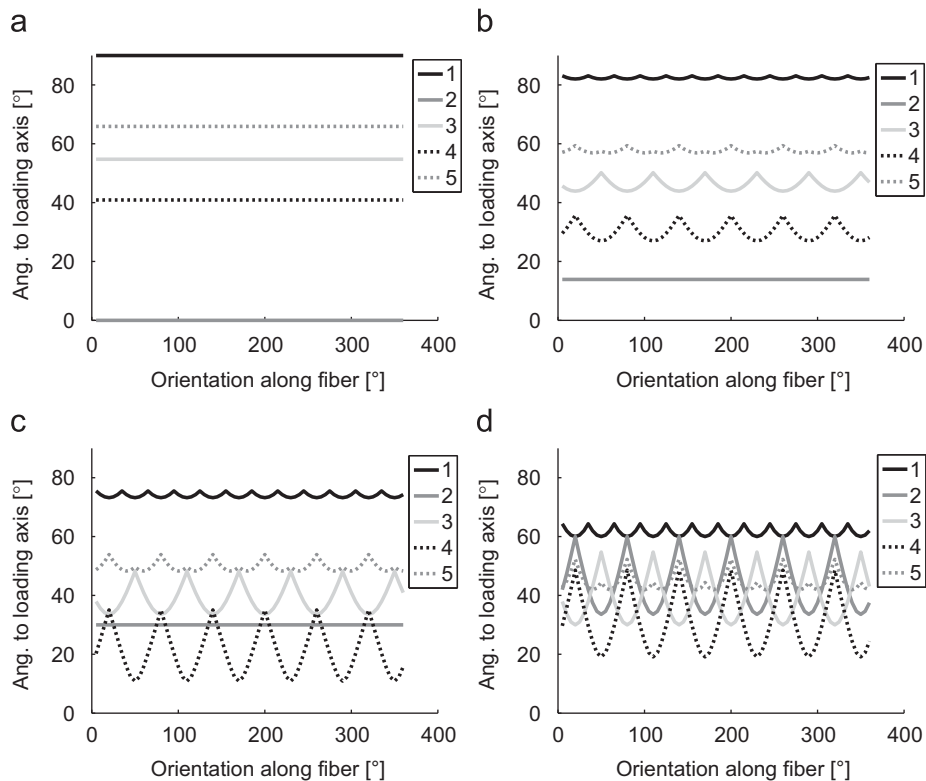

Fig. 4. For $\mathbf{R}_{\{1\,1\,1\}|[0\,0\,1]}$, ϕ_v^m is shown for each of the vertex families and an applied stress state varying from uniaxial tension along the z-axis ($\sigma_{xx}/\sigma_{zz} = 0$) to balanced biaxial tension in the x- and z-directions ($\sigma_{xx}/\sigma_{zz} = 1$). The legend refers to the vertex family number shown in Fig. 3. (a) $\sigma_{xx}/\sigma_{zz} = 0$. (b) $\sigma_{xx}/\sigma_{zz} = 0.25$. (c) $\sigma_{xx}/\sigma_{zz} = 0.5$. (d) $\sigma_{xx}/\sigma_{zz} = 1$.

in the x- and z-directions. Notice that in the uniaxial case where $\boldsymbol{s}$ of the fiber is aligned with the tension direction of the applied stress, ϕ_v^m, is independent of position along the fiber, but as the level of biaxiality increases a dependence is introduced between the coaxiality and the position along the fiber. With small levels of biaxiality, though the exact value of the coaxiality varies, the particular vertex family with the lowest value (i.e. that which is most highly aligned with the applied stress) remains the same. As the level of biaxiality increases that is no longer the case. In the balanced biaxial

situation, at some points along the fiber, vertex family 4 is most highly aligned and at some positions the closest is vertex family 3. In the uniaxial case it is always vertex family 2 (which agrees with the information presented in Fig. 3).

The information presented in Figs. 3 and 4 refers only to single crystals with particular orientations being subjected to specific ideal applied stresses. When the same analysis is applied to polycrystals, the situation complicates considerably. However, since crystal stresses should tend towards vertices in the SCYS as plastic deformation accumulates, in grains within polycrystals as well as in single crystals, Fig. 4 shows that we should expect to see a highly heterogeneous stress field, even among crystals along a single crystallographic fiber, in anything but the simplest macroscopic stress states. Another factor adding to the heterogeneity of stress in grains along the same fiber in a polycrystal, in addition to the different directions of the vertices in deviatoric stress space, is that the vertex families also have different magnitudes. In our constitutive model we assume that g^α grows uniformly for all slip systems (ignoring latent hardening). Because the vertex stresses are calculated on the basis of intersections of facets in the SCYS, as the SCYS expands the vertex stresses will extend in a constant proportion to each other. We can determine their relative magnitude by taking the norm of their vector representations, which are shown in Table 1. For example, we have seen that in the balanced biaxial case crystals along the $\mathbf{R}_{[1\,1\,1][1\,0\,0]}$ fiber should tend towards stress in either vertex family 3 or vertex family 4. Two neighboring crystals with very similar orientations might fall into these two separate conditions, in which case their relative stress magnitudes can be expected to differ by up to 30%.

4. Methodology for generating and analyzing stress in polycrystals

The previous sections have laid the groundwork for this study by introducing and defining crystal lattice orientations and stresses as well as the SCYS. So far we have dealt only with quantities involving single crystals and ideal applied stress states, which are directly calculable without using simulations of any kind. Here we present the methodology of data generation and analysis for studying the behavior of stresses in polycrystals. The data are generated using finite element simulations and are analyzed as distributions over the fundamental region of orientation space and over fibers through orientation space. We introduce both the numerical formulation of the simulations and the particulars of the simulations used in this study and provide details of the different analysis methods used.

4.1. Numerical formulation

The data we use to explore stresses on a crystal level as related to macroscopic stresses and yield surface vertices come from finite element simulations of the mechanical response of polycrystalline solids. The finite element formulation employs:

- a weak form of the equations of equilibrium;
- a large strain kinematic framework based on a multiplicative decomposition of the deformation gradient into plastic, rotational and elastic portions;
- anisotropic elastic behavior appropriate to the fcc crystal structure;
- anisotropic plastic behavior based on restricted slip of 12 $\{1\,1\,1\}\langle 1\,1\,0\rangle$ slip systems;
- rate-dependent slip with low rate sensitivity (rate insensitive behavior);
- strain hardening via integration of Voce-type equation for evolution of the slip system strengths;
- texture evolution via update of the lattice orientation in each finite element;
- traction or velocity boundary conditions; and
- a data parallel implementation.

A complete description of the formulation is available in several articles: Marin and Dawson (1998a, b) and Barton et al. (1999).

Model parameters for the elasticity and plastic behaviors representing a range of aluminum alloys as well as a stainless steel alloy have been used. In particular, the elastic moduli have been varied to modify the level of elastic anisotropy. Also, the slip system hardening has been varied, but only within the framework of a single strength value for all slip systems.

Table 1
Magnitude of the deviatoric vectorized form of each SCYS vertex family.

Vertex family number	Relative magnitude of ν
1	1.00
2	1.50
3	1.73
4	1.33
5	1.23

Within these limits, the distributions of crystal stresses have been found not to depend strongly on the choice of material parameters once fully developed plastic flow is reached under loading.

4.2. Loading the virtual polycrystals

The simulations are performed on virtual polycrystals. These are finite element meshes, initially cubic in shape, divided into distinct grains (or crystals). In this work, there are on the order of 1000 interior grains in each simulation mesh as well as a number of partial grains that complete the cube. Miller et al. (2008) have shown that this number of crystals is sufficient to accurately reflect the conditions and results in a physical polycrystal. A fully interior grain is a rhombic dodecahedron comprising 48 10-noded tetrahedral elements; incomplete grains near the boundary are formed from fewer elements. Grains are defined by neighboring elements (ones that share a common face) sharing an identical initial lattice orientation, which is set by random sampling from a uniform ODF.

Several loading histories, shown schematically in Fig. 5(a), have been simulated; results are shown for two, which are indicated in the figure. One set of results is for a virtual polycrystal deformed under uniaxial tension in the z-direction at a constant velocity. Results from the simulation including elemental stresses, strains and orientations were saved in both loaded and unloaded configurations, as shown schematically in Fig. 5(b). The unloaded configuration occurs when the virtual polycrystal has been deformed to a small amount of plastic strain (less than 10%) and then the elastic strain is relaxed. The second set of results is for a virtual polycrystal deformed under a balanced biaxial applied stress state through the application of traction boundary conditions on the x and z faces, generating $\sigma_{xx} = \sigma_{zz}$. The maximum strain in the x- and z-directions is about 7% to obtain fully developed plasticity in all the crystals of the mesh.

For both the uniaxial and biaxial cases symmetry boundary conditions were applied on three faces of the polycrystal; accordingly there are two and one faces, respectively, that are velocity- and traction-free. An example of a deformed mesh for the balanced biaxial simulation is represented in Fig. 6 where the tetrahedral elements of the mesh are colored according to the grain to which they belong. Note how the grains appear as "squares" on the exterior of the polycrystal but this is due to the fact that they are cut to give flat surfaces; in the image on the right the rhombic dodecahedral grain shape is perceivable. The mesh is elongated by almost the same quantity along the x- and z-directions, whereas a strong contraction in the y-direction develops due to the Poisson effect.

During analysis of the results, the macroscopic stress state, $\boldsymbol{\sigma}_{m}$, is always assumed to be either purely uniaxial with tension aligned in the mesh z-direction, or balanced biaxial tension in the x- and z-directions. The appropriateness of this simplification can be measured by considering the magnitude of the other stress components. In the uniaxial case, averaging the individual elemental stresses over the entire mesh results in non-zero but small values for the other stress components. The magnitudes of these components are generally less than 1% of the active (largest) stress component.

Though the finite elements initially share a common lattice orientation with other elements in the same grain, each element is allowed to deform and undergo lattice reorientation independently over the course of the loading. Therefore each element is considered individually when examining crystal stresses, $\boldsymbol{\sigma}_{c}$, together with its lattice orientation. The vertex stresses, $\boldsymbol{\sigma}_{v}$, which have fixed relation to the crystal bases as described in Section 3.3, also have different global orientations for each element as the loading proceeds and the lattice orientations evolve.

Calculating the coaxiality of a crystal stress to a vertex stress is done by applying the elemental orientation as well as all crystal symmetries to the vertex stress and taking the minimum ϕ_{v}^{c} over all of those symmetries.
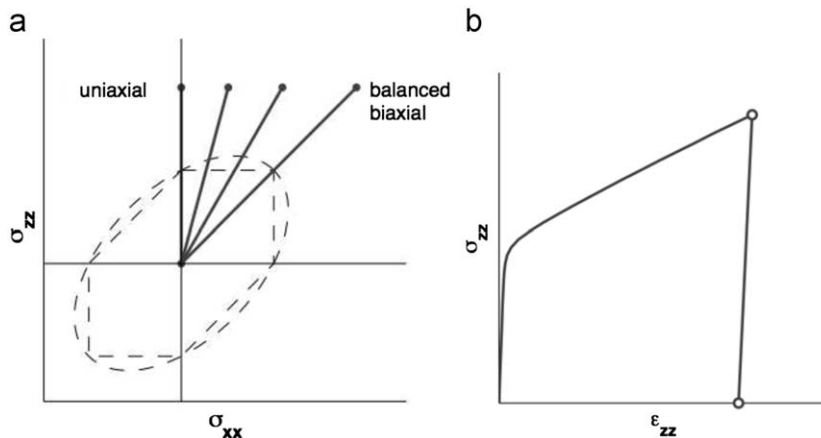

Fig. 5. Schematics of the macroscopic deformation from the simulations. (a) The balanced biaxial and the uniaxial conditions are indicated. The dashed lines represent the initial V.Mises and Tresca yield loci (load path in 2-D stress space for all simulations). (b) An example of a "loaded" and an "unloaded" condition are indicated by the circles (macroscopic stress-strain curve in the z-direction).
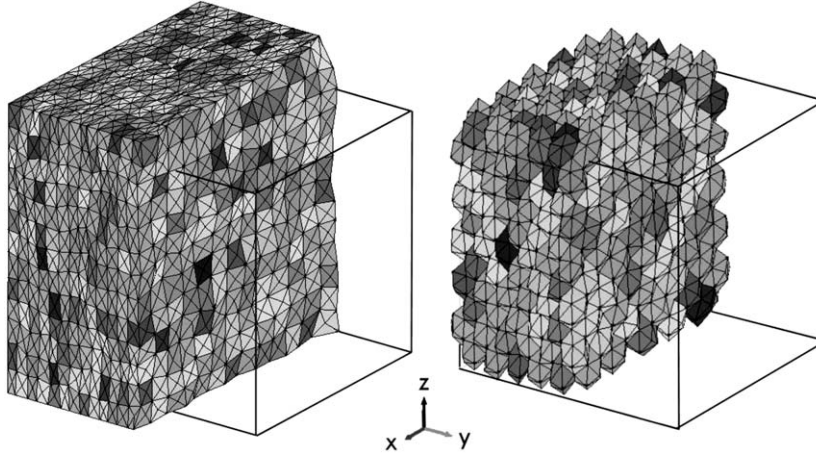
Fig. 6. Deformed mesh for the balanced biaxial simulation at maximum straining. The original undeformed cubic shape is represented by the black lines. The left image depicts the surface grains while the image on the right shows only complete grains composed of 48 tetrahedra. The deformation has been scaled to improve clarity.

4.3. Distributions over the fundamental region

We examine the orientational dependence of stress data by computing distributions over the fundamental region of Rodrigues space. For each variable of interest (e.g., each stress component or angle of coaxiality), a piecewise linear polynomial representation is used over the fundamental region based on a mesh with 254 unique nodes and 1512 4-node tetrahedral elements. To map data from the virtual polycrystal to the mesh over the fundamental region, each element from the virtual polycrystal is associated with the node in the fundamental region whose lattice orientation most closely matches its own. After all elements in the virtual polycrystal have been assigned to a node, there are anywhere from 50 to 800 values from the virtual polycrystal associated with every node in orientation space. Using these sets of nodal data, the average and standard deviation is computed for every node. The distribution over the fundamental region thus is defined from the complete set of nodal values together with the finite element interpolation functions.

4.4. Distributions associated with fibers

The elements contributing to a fiber are found by first calculating the misorientation angle, θ, between each element and $\mathbf{R}_{[c][s]}$ via Eq. (9), which requires that both c and s are first reduced to unit vectors:

$$\theta = \cos^{-1}(\mathbf{R}c \cdot s). \tag{9}$$

The misorientation angle is used to test if a crystal orientation lies close to a fiber (Barton and Dawson, 2001). When calculating θ we apply all crystal symmetries $\mathbf{R}^{\mathrm{sym}}$ to the orientation of the element and test each resulting orientation, saving only the equivalent orientation which results in the lowest value of θ. Once the misorientation is found between each element's lattice and the desired fiber, a cutoff of a certain allowable misorientation is used to decide if an element's lattice lies on the fiber. We generally use $\theta < 5°$ as the criterion. This is larger than a typical value from diffraction experiments, but is necessary for a reasonable number of elements to be associated with a fiber given the number of crystals in the virtual polycrystal. Elements can now be treated in groups by fiber, which is similar to the way crystals are grouped during data collection in diffraction experiments, as discussed in Section 2.2.

5. Stress distributions over the fundamental region

We examine first the orientation dependence of the crystal stresses at-large by mapping the stresses from the virtual polycrystal undergoing fully plastic deformation to the fundamental region according to the procedure described in Section 4.3. Because the yield condition depends on the deviatoric part of the stress and does not depend on the mean part, we plot these separately. To examine the connection of the stresses to the vertices of the SCYS, we show the coaxiality first between the crystal stresses and the macroscopic stress and then between the crystal stresses and the closest vertex stress. Comparison of the stress and coaxiality distributions to the positions of fibers motivates exploiting the fibers to interpret the dependence of crystal stress on orientation.

The stress, both its magnitude and the direction, experienced by any grain in a polycrystal aggregate is due to a combination of factors, including the macroscopic stress state, the orientation of the grain (which effects its apparent stiffness), and its neighborhood. Even for such a seemingly simple macroscopic stress state as uniaxial tension, significant
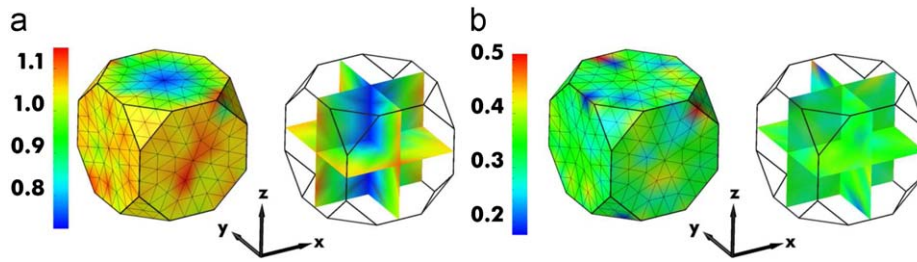
Fig. 7. Average stress magnitudes, normalized by the J2-effective macroscopic stress, shown throughout orientation space for the case of uniaxial macroscopic loading in the *z*-direction. The value at each point in orientation space is the average of all elements sharing that orientation. (a) Average normalized deviatoric stress. (b) Average normalized pressure.
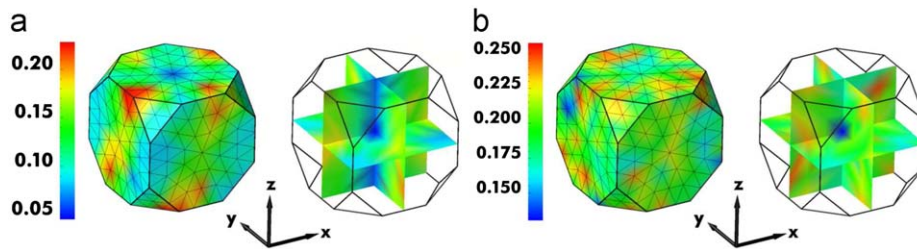

Fig. 8. Standard deviation of stress magnitudes, normalized by the J2-effective macroscopic stress, shown throughout orientation space for the case of uniaxial macroscopic loading in the *z*-direction. The value at each point in orientation space is due to all elements sharing that orientation. (a) Standard deviation of normalized deviatoric stress. (b) Standard deviation of normalized pressure.

stress variation can exist, both between the various grains in the bulk and within individual grains. The distributions shown here have been generated numerically. Consequently, we expect that the distributions will reflect the underlying theory and, at least to some extent, will show a link between the stress and the single crystal yield surface. Factors such as the spatial heterogeneity in stress stemming from local neighborhood effects could mask this dependence if those factors are sufficiently strong. Thus, before applying these results to actual materials, we need to consider the issue of whether the model is sufficiently true. This point has been examined by Miller et al. (2008) in a comparison of experimentally measured[2] and computed stress distributions using the same numerical formulation employed here. Quantitative comparisons were conducted on the basis of expansions of the distributions for each component of the stress using spherical harmonics. It was found that the dominant (non-zero) modes for experiment and simulation were the same and their magnitudes compared favorably for the majority of the cases examined.

Shown in Fig. 7 are the variations in the magnitude of the deviatoric stress (Fig. 7(a)) and the pressure (Fig. 7(b)) for a mesh under uniaxial loading.[3] The values shown are from the elemental stresses normalized by the effective macroscopic stress from the simulation. This normalization is to ease comparison of simulations performed with different material parameters. The magnitude of the deviatoric stress is systematically related to crystal orientation, with the stress having greater magnitude in crystals whose coordinate axes are less closely aligned with the sample tension axis. The range in values corresponds approximately to range in vertex stresses for the different vertex families: the ratio of maximum to minimum values is 1.73 for the vertex stress magnitudes and approximately 1.6 for the average deviatioric stress magnitudes (averaging in the mapping of data to the fundamental region tends to smooth the distribution and diminish the range). The variations in average pressure throughout orientation space are comparable to those of the deviatoric stress, but are not systematically related to orientation.

The variation in the average of the magnitude of the deviatoric stress over the fundamental region is larger than the standard deviation at any particular orientation, as can be seen by comparing Figs. 7(a) and 8(a). Recall that each node in the orientation space mesh represents simulation results from between approximately 50 and 800 elements. Fig. 8(a) shows the standard deviation of the deviatoric stress magnitude in the uniaxial loading over all the elements contributing to each point in orientation space, again normalized by the effective macroscopic stress. The standard deviation has a smaller magnitude range and a distinctly different pattern from the average of the deviatoric stress. There is orientational dependence, but more specifically, it relates to the fiber on which a crystal orientation lies. These data demonstrate that

---

[2] The experiments measure the elastic strain tensor, which is subsequently converted to stress using the elastic moduli for cubic crystals.

[3] The plots in Figs. 7–11 display the values of a field over the surface of the fundamental region (left) and within its interior over three coordinate planes (right).
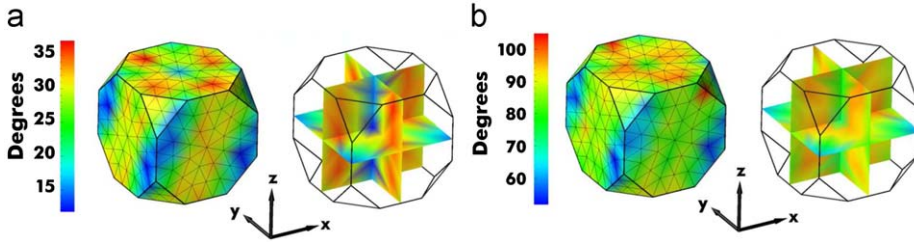
Fig. 9. Average angle of coaxiality between crystal stresses and the macroscopic stress, ϕ_c^m, shown throughout orientation space for both the loaded and unloaded configurations of the uniaxial simulation. (a) Loaded state. (b) Unloaded state.
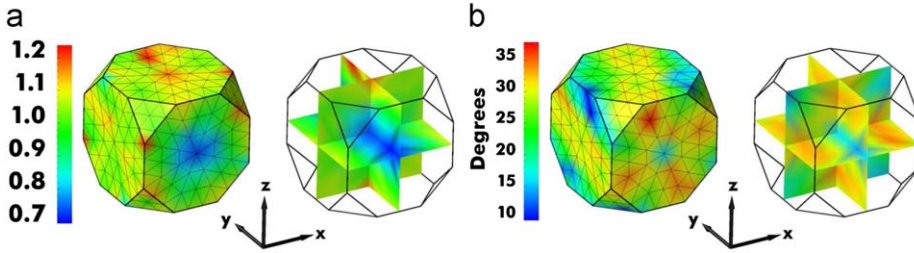

Fig. 10. Average deviatoric stress, normalized by the J2-effective macroscopic stress, and ϕ_c^m shown throughout orientation space for the balanced biaxial tension simulation. (a) Normalized deviatoric stress. (b) ϕ_c^m.
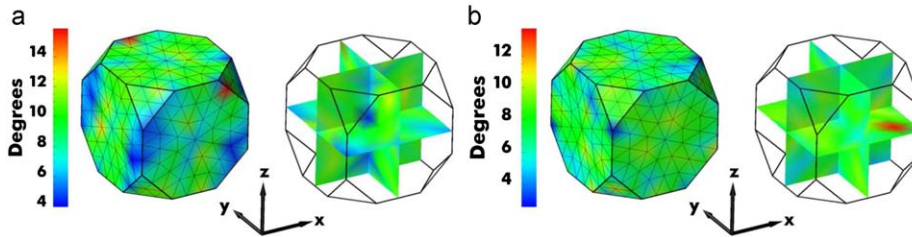

Fig. 11. Average angle of coaxiality between crystal stresses and the nearest SCYS vertex stress, ϕ_c^v, shown throughout orientation space. (a) Uniaxial tension. (b) Balanced biaxial tension.

while the neighborhood does have an important impact on the stresses in crystals, as seen in the standard deviation of stress among crystals with nominally the same orientation, the more significant cause of stress variation within a polycrystal is due to crystal orientations themselves.

The patterns in Fig. 8(a) echo the fibers in Fig. 1. The pattern is even more evident in Fig. 9(a), which shows ϕ_c^m for the domain under load, again in the uniaxial tension case. Specifically, the 100 fiber exhibits low stress, low stress variation, and low ϕ_c^m; the 111 fiber exhibits high stress, relatively low stress variation, and low ϕ_c^m; both the 110 and 311 fibers have both high ϕ_c^m and relatively high stress and stress variation. Both the standard deviation of deviatoric stress magnitude and the values of ϕ_c^m are lower for those crystals associated with $\mathbf{R}_{\{1\,1\,1\}[0\,0\,1]}$ and $\mathbf{R}_{\{1\,0\,0\}[0\,0\,1]}$, which is reasonable since a lower value of ϕ_c^m indicates a higher level of alignment between the crystal and macroscopic stresses, and stresses that are more highly aligned with the macroscopic stress have less source of variation. Similar trends are evident in the balanced biaxial stress case, as Fig. 10 shows. In this case the macroscopic stress is isotropic in the $x-z$ plane, so the fibers that appear evident in Fig. 10(b) are $\mathbf{R}_{\{c\}[0\,1\,0]}$.

Figs. 7–9(a) show results for the highest macroscopic stress throughout the uniaxial deformation. The stresses in the unloaded state also exhibit patterns related to crystal orientation. In the unloaded state the crystal stresses are no longer on the yield surface and therefore need not have any relation to the vertex stresses; this is played out in Fig. 9(b), which shows most crystals having deviatoric stress states more perpendicular than parallel to the macroscopic deviatoric stress. The range of values of ϕ_c^m in the unloaded condition as compared to the loaded condition further strengthens our contention that those patterns and values in the loaded condition are significant. The crystals are certainly tending towards very specific values of coaxiality to the macroscopic stress when the polycrystal is undergoing plastic deformation.

Having seen that ϕ_c^m can be as high as 35°, compare ϕ_c^v in Fig. 11 which shows the coaxiality between the crystal stresses and whichever SCYS vertex is most closely aligned, regardless of which vertex that is. The range of values is much smaller,

at 10° or less, throughout most of orientation space for both the uniaxial and biaxial stress cases. Considering that the minimum value of coaxiality between crystal stresses and macroscopic stresses is in range of the maximum value of coaxiality between crystal stresses and most highly aligned vertex stresses over much of orientation space, the data present compelling evidence that crystal stresses are dictated primarily by the SCYS and its vertices. Looking at the relative uniformity of ϕ_c^v in Fig. 11 compared to ϕ_c^m in Figs. 9(a) and 10(b) (a range of around 10° or less in the former and 20° or more in the latter) indicates that all crystal stresses have an equal tendency towards the nearest SCYS vertex but that examining the data by looking along crystallographic fibers should reveal further information about the crystal stresses themselves, specifically relating to which vertices are active for different fibers.

6. Relation of crystal and vertex stresses on fibers

The results of the previous section indicate that analysis of these data with respect to fibers is a reasonable undertaking. Since crystals contributing to the same diffraction measurements (i.e. satisfying the same Bragg condition) are those crystals sharing a common orientation up to rotation about the crystal direction, analysis along fibers is desirable even without considering the indications of the previous section. In *in situ* diffraction experiments on bulk specimens it is often difficult to separate results from the various crystals contributing to each measurement. Most analysis therefore depends on treating those crystals as indistinguishable. The following results, however, show the shortfall of such a treatment.

Fig. 12 shows a histogram of ϕ_c^v for several fibers in the uniaxial macroscopic stress case, indicating each element's distance to the most closely aligned vertex family, and also includes a histogram of which vertex family generates that value. These data are for the peak load in the simulation, at approximately 8% specimen strain, with fully plastic deformation taking place. Compare Fig. 12 to Fig. 3. The most frequent vertex family for each fiber in Fig. 12 matches the vertex family in Fig. 3 with the smallest value of ϕ_v^m for that fiber. Recall that Fig. 3 has been generated independently from the simulations of the virtual polycrystals. The coaxialities in that figure are based solely on crystal orientation for each
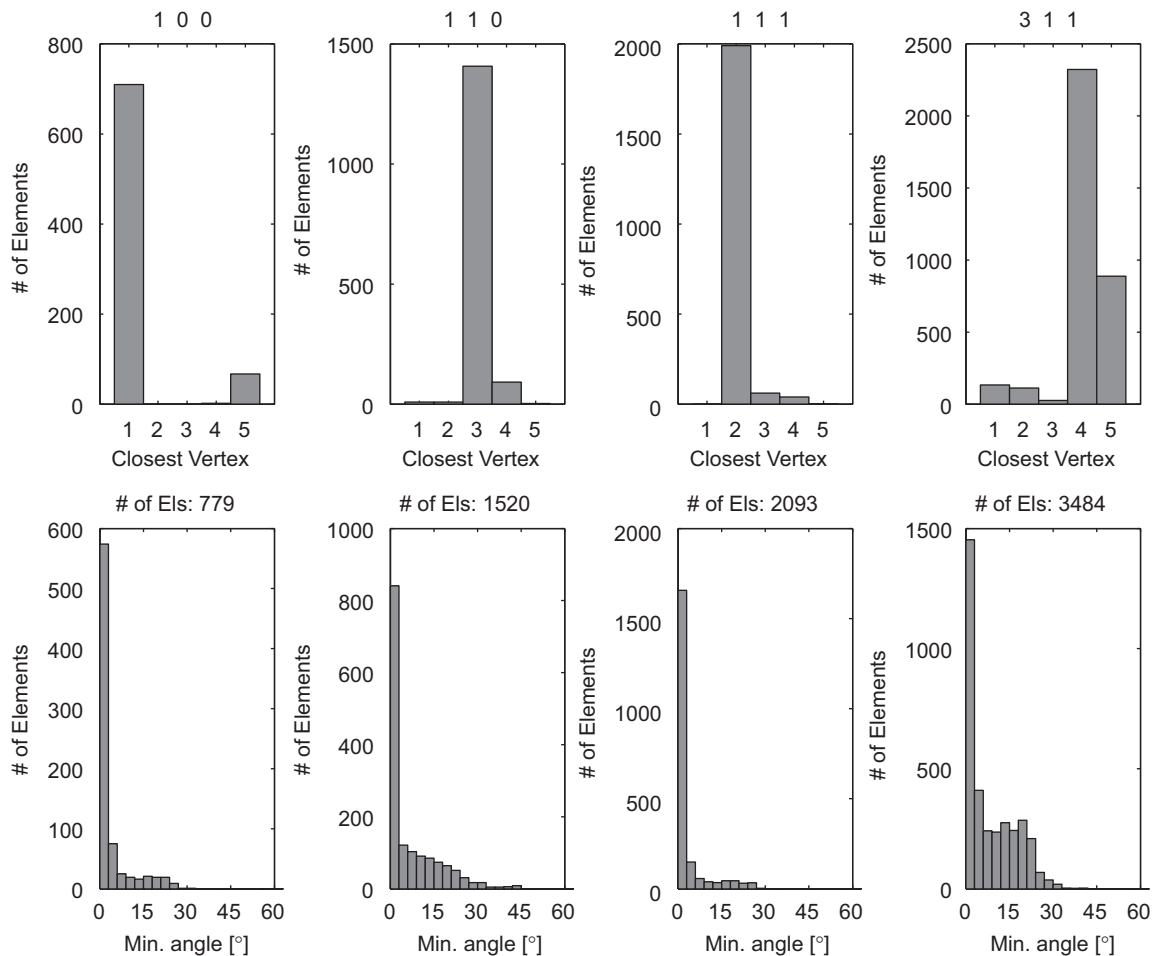

Fig. 12. Histograms of the nearest vertex family (top) and ϕ_c^v for that family (bottom) for crystal stresses from four fibers in the uniaxial case.

fiber and SCYS vertices which are tied to the crystal lattice, along with an assumed applied macroscopic stress state. In contrast, the coaxialities in Fig. 12 are calculated directly from the simulation results. Each element has a particular orientation, and using that orientation and the stress which results from the simulation, ϕ_c^v is calculated. The stresses tend towards the vertex family that is most closely aligned with the macroscopic stress state, which confirms the assumption that crystal stress will tend towards SCYS vertices and will be only as closely aligned with the macroscopic stress as is possible given the vertices on the crystal SCYS. Certain fibers have more variation than others in terms of which vertex is most likely to be active. This corresponds to the fibers that have no vertex particularly well aligned with the macroscopic stress, i.e. $\mathbf{R}_{\{1\,1\,0\}[0\,0\,1]}$ and $\mathbf{R}_{\{3\,1\,1\}[0\,0\,1]}$. In the case of the $\mathbf{R}_{\{3\,1\,1\}[0\,0\,1]}$ fiber, the elements divide between two vertex families and there is a broader tail to the colinearity distribution, especially in comparison to the fibers with a single vertex family that is well-aligned with the macroscopic stress. A general trend is that the standard deviation of the crystal stresses of elements contributing to a fiber is smaller if that fiber has a single well-aligned family of vertices.

Turning now to the balanced biaxial stress case, Fig. 13 shows results for fibers with the scattering vector in the y-direction. Recall that this scattering vector is normal to a plane with isotropic stress. Figs. 13 and 12 appear almost identical, as expected since Fig. 3 applies to this case as well. Fibers with scattering vectors in the z-direction, however, exhibit much different behavior, as shown in Fig. 14. While the coaxiality angles between crystal stress and vertex stresses are universally small, the particular family into which crystals on each fiber fall shows much more variation. Compare results for each fiber in Fig. 14 to Fig. 15, which shows the same information as Fig. 4(d) but for all of the crystal directions considered here. For example, look at the information for the 111 fiber. At various positions along that fiber vertex family 4 has the smallest angle of coaxiality to the macroscopic stress, and at other positions vertex family 3 is closest. Those are indeed the vertices into which the crystal stresses align themselves in the simulation. The same analysis holds true for each of the fibers presented here.
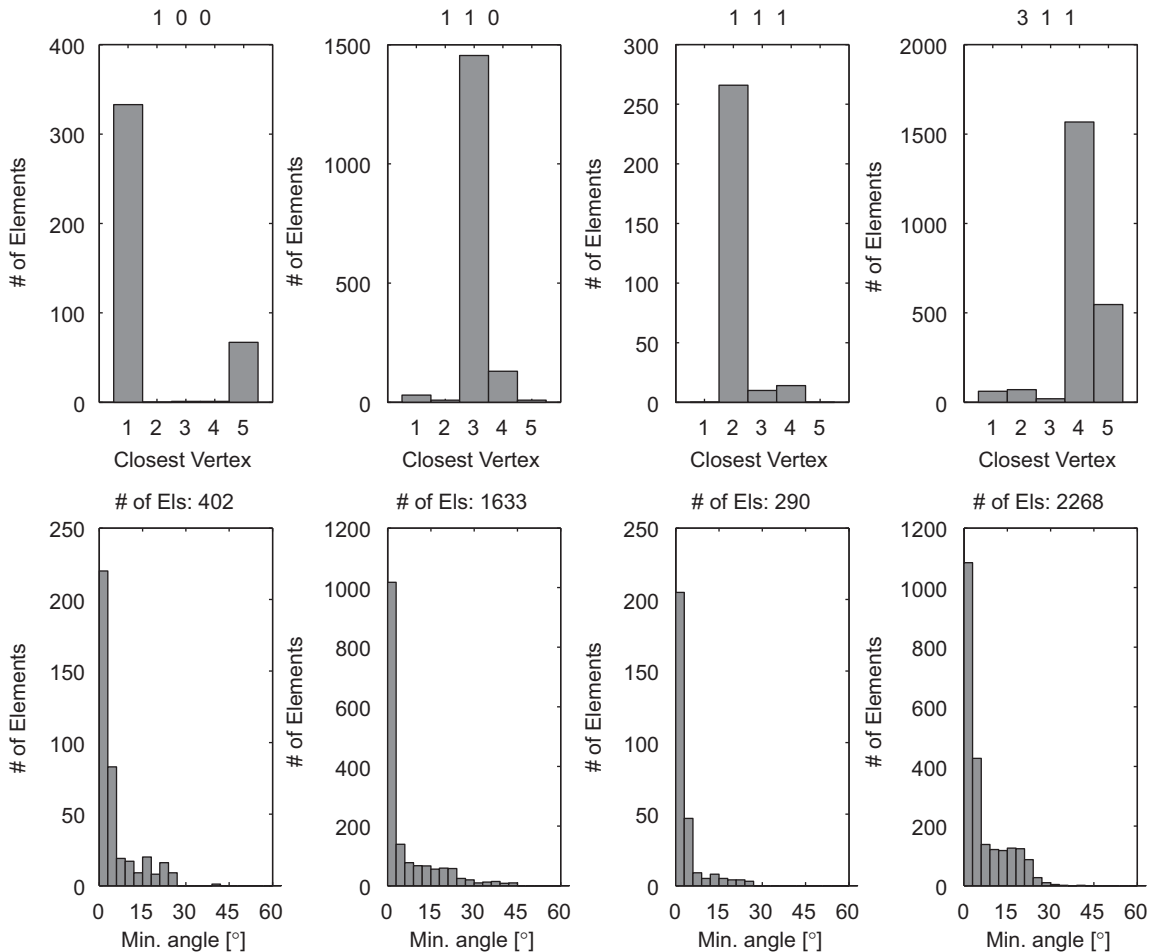

Fig. 13. Histograms of the nearest vertex family (top) and ϕ_c^v for that family (bottom) for crystal stresses from four fibers with scattering vectors in the y-direction of the balanced biaxial case.
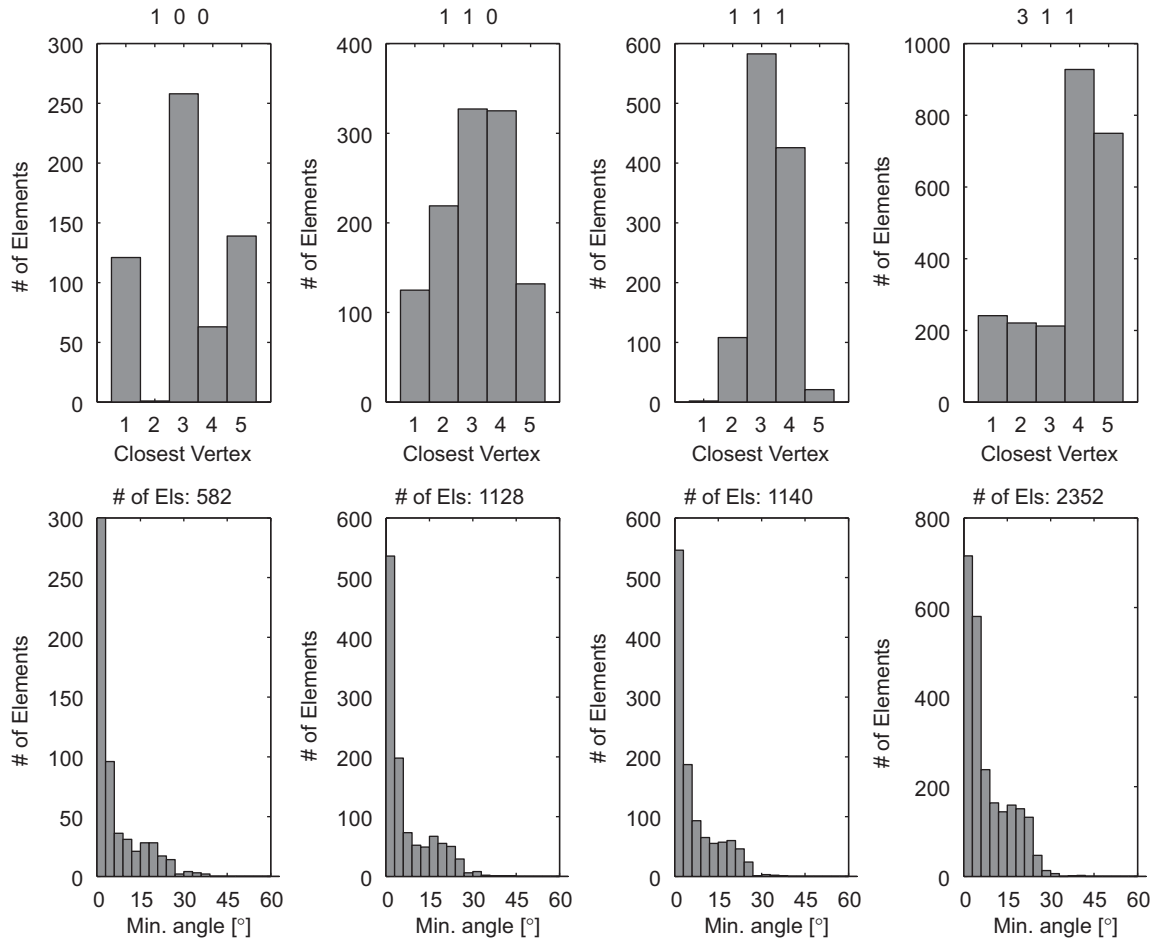
Fig. 14. Histograms of the nearest vertex family (top) and ϕ_c^v for that family (bottom) for crystal stresses from four fibers with scattering vectors in the z-direction of the balanced biaxial case.

7. Discussion

The results presented in the preceding sections of the paper demonstrate in several ways the influence of the geometry of the single crystal yield surface on the crystal stress distributions. The yield surface is formed from the inner envelope of hyperplanes in deviatoric stress space. The consequence of the plastic straining direction satisfying normality to the surface is that most stress states will lie in a vertex, or possibly on an edge, as it is unlikely that the plastic straining direction will correspond precisely with one of the facet normal directions. Kinetics of plastic flow alter the picture somewhat by rounding the features of the rate-independent polytope. However, as materials are often rate insensitive over a large regime of strain rate and temperature, the rounding is slight and the picture from the rate-independent idealization is accurate. This is what is demonstrated by the results presented here, confirming the description advanced by Kocks and co-workers in a series of papers (Kocks, 1960, 1970; Kocks et al., 1983). Finite element simulations of polycrystals introduce the effects of spatial arrangement of crystals over the models employed by Kocks. During plastic flow, stresses do migrate to the SCYS vertices in finite element simulations as indicated in earlier publications by Maniatty and Yu (1996) and by Barton et al. (1999). Here we extend the documentation of that behavior by quantifying the proximity of the crystal stresses to vertex stresses using distributions of the coaxiality over the fundamental region of orientation space. Moreover, the degree of misalignment between the vertex stresses and the macroscopic stress, together with the preferred alignment of the crystal stresses with the vertex stresses, serves to quantify the variations in crystal stresses with orientation during plastic flow. These variations are substantial and have been shown to be in good agreement with measured variations in deforming copper (Miller et al., 2008). The SCYS continues to have a bearing on the crystal stress distribution following unloading as the unloaded stress distribution inherits orientational dependence from the stress distribution under load. This is evident in the comparison of Fig. 9(a) with Fig. 9(b).

One of the main implications of the stress distributions is for the interpretation of diffraction data for lattice strains in terms of diffraction moduli. Diffraction moduli relate the change in average lattice strain taken over a fiber to the change in
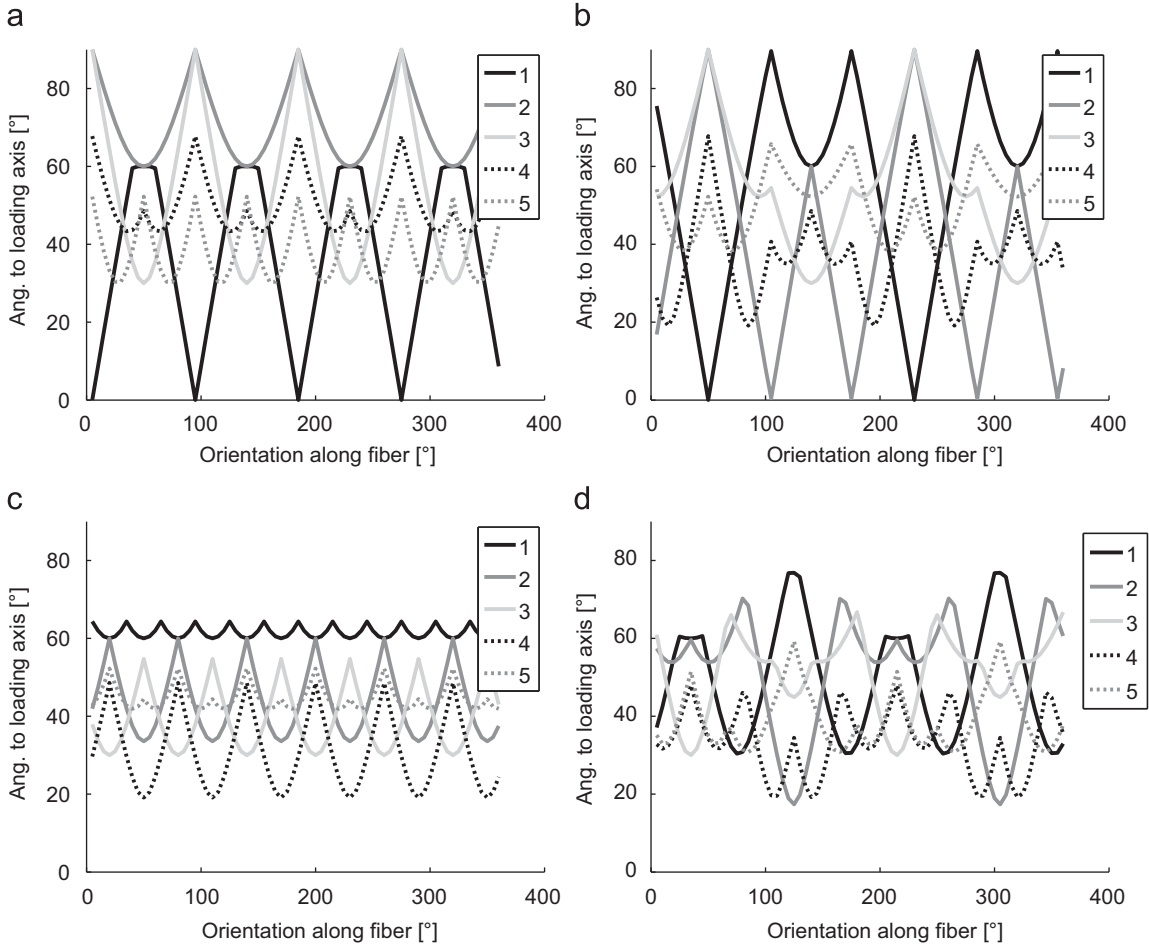
Fig. 15. For each fiber with axial scattering vectors in the balanced biaxial case, ϕ_v^m is shown as a function of position along the fiber. Note that this plot refers only to single crystals oriented along these fibers and is not generated from polycrystal simulation data. (a) $\mathbf{R}_{\{1\,0\,0\}[0\,0\,1]}$. (b) $\mathbf{R}_{\{1\,1\,0\}[0\,0\,1]}$. (c) $\mathbf{R}_{\{1\,1\,1\}[0\,0\,1]}$. (d) $\mathbf{R}_{\{3\,1\,1\}[0\,0\,1]}$.

macroscopic stress. Often there is an assumption made in interpreting the moduli that the macroscopic stress and the crystal stress are equal. The results presented in the preceding sections clearly indicate that this is not the case, with crystal stresses tending towards the vertex stress once plastic flow occurs. In general, neither the direction nor the magnitude of the crystal stress coincide with the macroscopic stress. Instead, there usually is a mix of cases, with close coaxiality between the macroscopic stress and the vertex stress for some fibers and not for others. Further, even among fibers in which the vertex and macroscopic stresses are aligned, the magnitudes of the stresses differ. These differences affect the interpretation of the diffraction data, especially conclusions regarding the strength of the elastic anisotropy, as discussed in Ritz (2008). The situation is made more complex by the introduction of texture. Stronger textures will more heavily weight some orientations over others, altering the relative importance of crystals associated with different fibers. If fibers with close alignment of the vertex and macroscopic stresses have volume fractions of crystals that are elevated above values for a uniform texture, the assumption that crystal stresses equal the macroscopic stress might be more accurate. On the other hand, if the texture is weak along these fibers, then this assumption might be less accurate.

Any one crystal of a polycrystal sits among grains having different lattice orientation and imparting a heterogeneous neighborhood. The neighborhood of grains defines the anisotropic medium through which a crystal is loaded and is unique to each randomly arranged crystal in a virtual polycrystal. This is evident in the results through the standard deviations of crystal stresses, both deviatoric and mean parts, shown in Figs. 8(a) and 8(b). While the variations in the average crystal stresses are not sufficient to completely mask the dependence of the average crystal stress on orientation, neither are they inconsequential. Thus, stress-driven processes like texture evolution that tend to follow trends governed by the average stress are predicted reasonably well. However, care should be exercised in using the averages to investigate other processes that depend more on extreme values of the active stress, like damage initiation. In these simulations the virtual polycrystals possess over 1000 interior grains which are discretized with approximately 50 000 higher-order tetrahedral elements. The stress varies considerably over these representations of a polycrystal. For the case of uniaxial tension, the ratio of the maximum to minimum deviatoric stress magnitude was approximately 3.4. This is notably larger than the ratio

of the vertex stress magnitudes (1.73) and ratio of the maximum to minimum average deviatoric stress (1.6), as discussed in Section 5. Thus, we emphasize that while there is an orientation dependence from the SCYS seen in the crystal stress distributions, the lattice orientation is not sufficient by itself to determine the crystal stress in plastically deforming polycrystals. We also point out that the statistics were gathered from simulations on virtual polycrystals having random lattice assignments from uniform orientation distributions. The strength of these trends may differ for textured polycrystals as the introduction of preferred orientations for the crystal lattices will influence the nature of the local neighborhood surrounding each grain.

8. Conclusions

The distributions of crystal stresses over orientation space have been simulated in polycrystal aggregates deformed under uniaxial and balanced biaxial tension into the regime of fully developed plastic flow. The computed crystal stresses are compared to stress states defined by vertices of the single crystal yield surface (vertex stresses). To accomplish this, the full set of vertex stresses is partitioned into five families such that from crystal symmetry the vertices in any one family are indistinguishable from others of the same family. The directions of the crystal stresses are compared to the directions of the vertex stresses based on the angle between their respective five dimensional vectors, referred to as their coaxiality. The results show that once the deformation has entered the plastic regime, crystal stresses tend to align with vertices of the single crystal yield surface and the coaxiality angle tends toward zero. The orientation of the most active vertex family depends on the orientation of the crystal lattice, implying that the stress active in a plastically deforming crystal tends to align with a vertex stress instead of the macroscopic, or nominal, stress if the two are not coincident. Further, for a specified stress state, the orientation dependence observed is seen to correlate with crystallographic fibers because along a fiber some vertex families, often just a single family, align more closely with the applied stress. The more one vertex family dominates this arrangement, the more tightly grouped are the crystal stresses in coaxiality with a vertex stress. The results emphasize the importance of the lattice orientation on the spatial variability of the stress of a polycrystal. In addition, the results show how the systematic dependence of crystal stress on orientation influence bulk diffraction measurements through their close association with crystallographic fibers via Bragg's law.

Acknowledgments

Appendix A. Coaxiality of vertex stress to macroscopic stress along a fiber

In some situations the coaxiality between a vertex stress state and an applied macroscopic stress state in a single crystal are independent of the crystal's particular orientation along a fiber. This may be true for certain fibers only or for all choices of c for a given s. That latter situation in particular is interesting to consider since it provides the most straightforward avenue of studying the relationships between vertex, crystal, and macroscopic stress states. Determining the (σ_m, s) combinations that result in such a situation proceeds as follows.

For any $\mathbf{R}_1$ and $\mathbf{R}_2$ along a fiber $\mathbf{R}_{[c][s]}$ the macroscopic stress written in the crystal framework must be identical. This ensures that the projection of the macroscopic stress against a vertex stress will be the same for all orientations along the fiber. Therefore,

$$\mathbf{R}_1^{\mathsf{T}}\sigma_m\mathbf{R}_1 = \mathbf{R}_2^{\mathsf{T}}\sigma_m\mathbf{R}_2, \tag{A.1}$$

$$\sigma_m\mathbf{R}_1\mathbf{R}_2^{\mathsf{T}} = \mathbf{R}_1\mathbf{R}_2^{\mathsf{T}}\sigma_m. \tag{A.2}$$

By defining $\mathbf{Q} = \mathbf{R}_1\mathbf{R}_2^{\mathsf{T}}$, Eq. (A.2) can be rewritten as

$$\sigma_m\mathbf{Q} = \mathbf{Q}\sigma_m, \tag{A.3}$$

where $\mathbf{Q}$ is any rotation whose axis is s. Note that $\mathbf{Q}s = \mathbf{R}_1\mathbf{R}_2^{\mathsf{T}}s = \mathbf{R}_1 c = s$, and s is an eigenvector of $\mathbf{Q}$ with corresponding eigenvalue $\lambda = 1$. The condition on σ_m from Eq. (A.3) is that it commute with any $\mathbf{Q}$. If that is the case, then

$$\sigma_m s = \sigma_m\mathbf{Q}s, \tag{A.4}$$

$$\sigma_m s = \mathbf{Q}\sigma_m s, \tag{A.5}$$

which shows that $\sigma_m s$ is also an eigenvector of $\mathbf{Q}$ with the corresponding eigenvalue $\lambda = 1$. Since most rotations $\mathbf{Q}$ will have eigenvalues of multiplicity 1 and the preceding analysis must be true for every $\mathbf{Q}$ having axis s, $\sigma_m s$ must be parallel to s, and s is an eigenvector of σ_m as well, with eigenvalue λ_1. Since σ_m is a symmetric matrix its eigenvectors are all

mutually orthogonal. Focussing now on the two-dimensional subspace orthogonal to $\boldsymbol{s}$, the requirement of commutation still holds. Letting σ_{aa}, σ_{bb}, and σ_{ab} represent the three components of $\boldsymbol{\sigma}_\mathrm{m}$ in that subspace and c_θ and s_θ represent the cosine and sine of the rotation angle of $\mathbf{Q}$ in that subspace,

$$\begin{bmatrix} \sigma_{aa} & \sigma_{ab} \\ \sigma_{ab} & \sigma_{bb} \end{bmatrix} \begin{bmatrix} c_\theta & -s_\theta \\ s_\theta & c_\theta \end{bmatrix} = \begin{bmatrix} c_\theta & -s_\theta \\ s_\theta & c_\theta \end{bmatrix} \begin{bmatrix} \sigma_{aa} & \sigma_{ab} \\ \sigma_{ab} & \sigma_{bb} \end{bmatrix}. \tag{A.6}$$

Carrying out the multiplication results in

$$s_\theta \begin{bmatrix} 2\sigma_{ab} & -\sigma_{aa}+\sigma_{bb} \\ -\sigma_{aa}+\sigma_{bb} & -2\sigma_{ab} \end{bmatrix} = 0, \tag{A.7}$$

which is true if and only if $s_\theta = 0$ or $\sigma_{aa} = \sigma_{bb}$ and $\sigma_{ab} = 0$. The former is the trivial case of a rotation of an integer multiple of π, but the latter is the case where

$$\boldsymbol{\sigma}_\mathrm{m} = \lambda_2 \mathbf{I} \tag{A.8}$$

on the plane, i.e. $\boldsymbol{\sigma}_\mathrm{m}$ is isotropic in the plane perpendicular to the scattering vector of the fiber.

Having shown that a stress state that commutes with a rotation $\mathbf{Q}$ having axis $\boldsymbol{s}$ satisfies $\boldsymbol{\sigma}_\mathrm{m}\boldsymbol{s} = \lambda_1\boldsymbol{s}$ and $\boldsymbol{\sigma}_\mathrm{m}\boldsymbol{t} = \lambda_2\boldsymbol{t}$ for $\boldsymbol{t} \perp \boldsymbol{s}$, let $\boldsymbol{v} = \alpha_1\boldsymbol{s} + \alpha_2\boldsymbol{t}$. Then,

$$\boldsymbol{\sigma}_\mathrm{m}\mathbf{Q}\boldsymbol{v} = \boldsymbol{\sigma}_\mathrm{m}(\alpha_1\mathbf{Q}\boldsymbol{s} + \alpha_2\mathbf{Q}\boldsymbol{t}) \tag{A.9}$$

$$= \alpha_1\lambda_1\boldsymbol{s} + \alpha_2\boldsymbol{\sigma}_\mathrm{m}\mathbf{Q}\boldsymbol{t} \tag{A.10}$$

$$= \alpha_1\lambda_1\boldsymbol{s} + \alpha_2\lambda_2\mathbf{Q}\boldsymbol{t}. \tag{A.11}$$

The final term in Eq. (A.11) results since $\mathbf{Q}$ is a rotation about $\boldsymbol{s}$ and $\mathbf{Q}$ acting on any vector perpendicular to $\boldsymbol{s}$ results in another vector perpendicular to $\boldsymbol{s}$. Considering now the commuted case of Eq. (A.9),

$$\mathbf{Q}\boldsymbol{\sigma}_\mathrm{m}\boldsymbol{v} = \mathbf{Q}(\alpha_1\boldsymbol{\sigma}_\mathrm{m}\boldsymbol{s} + \alpha_2\boldsymbol{\sigma}_\mathrm{m}\boldsymbol{t}) \tag{A.12}$$

$$= \alpha_1\lambda_1\boldsymbol{s} + \alpha_2\lambda_2\mathbf{Q}\boldsymbol{t}. \tag{A.13}$$

Comparing Eqs. (A.11) and (A.13) shows that $\mathbf{Q}$ and $\boldsymbol{\sigma}_\mathrm{m}$ commute, as required.

References

Altmann, S.L., 1986. Rotations, Quaternions, and Double Groups. Dover Publications, Mineola, NY.

Arminjon, M., 1991. A regular form of the Schmid law, application to the ambiguity problem. Textures and Microstructures 14–18, 1121–1128.

Barton, N., Dawson, P., Miller, M., 1999. Yield strength asymmetry predictions from polycrystal elastoplasticity. Journal of Engineering Materials and Technology 121, 230–239.

Barton, N.R., Benson, D.J., Becker, R., 2005. Crystal level continuum modelling of phase transformations: the $\alpha \leftrightarrow \varepsilon$ transformation in iron. Modelling and Simulation in Materials Science and Engineering 13 (5), 707–731.

Barton, N.R., Dawson, P.R., 2001. A methodology for determining average lattice orientation and its application to the characterization of grain substructure. Metallurgical and Materials Transactions A 32 (8), 1967–1975.

Beausir, B., Tóth, L.S., Neale, K.W., 2007. Role of strain-rate sensitivity in the crystal plasticity of hexagonal structures. International Journal of Plasticity 23 (2), 227–243.

Becker, R., Panchanadeeswaran, S., 1989. Crystal rotations represented as Rodrigues vectors. Textures and Microstructures 10, 167–194.

Bernier, J.V., Miller, M.P., 2006. A direct method for the determination of the mean orientation dependent elastic strains and stresses in polycrystalline alloys from strain pole figures. Journal of Applied Crystallography 39 (3), 358–368.

Bishop, J.F.W., 1953. A theoretical examination of the plastic deformation of crystals by glide. Philosophical Magazine 44, 51–64.

Bridier, F., McDowell, D.L., Villechaise, P., Mendez, J., 2009. Crystal plasticity modeling of slip activity in Ti–6Al–4V under high cycle fatigue loading. International Journal of Plasticity 25 (6), 1066–1082.

Busso, E.P., Cailletaud, G., 2005. On the selection of active slip systems in crystal plasticity. International Journal of Plasticity 21 (11), 2212–2231.

Canova, G.R., Kocks, U.F., Tomé, C.N., Jonas, J.J., 1985. The yield surface of textured polycrystals. Journal of the Mechanics and Physics of Solids 33 (4), 371–397.

Chu, T.C., Ranson, W.F., Sutton, M.A., Peters, W.H., 1985. Applications of digital-image-correlation techniques to experimental mechanics. Experimental Mechanics 25 (3), 232–244.

Clausen, B., Lorentzen, T., 1997. Experimental evaluation of a polycrystal deformation modeling scheme using neutron diffraction measurements. Metallurgical and Materials Transactions A 28A (12), 2537–2541.

Conti, S., Hauret, P., Ortiz, M., 2007. Concurrent multiscale computing of deformation microstructure by relaxation and local enrichment with application to single-crystal plasticity. Multiscale Modeling and Simulation 6 (1), 135–157.

Conti, S., Ortiz, M., 2005. Dislocation microstructures and the effective behavior of single crystals. Archive for Rational Mechanics and Analysis 176 (1), 103–147.

Cuitino, A.M., Ortiz, M., 1992. Computational modelling of single crystals. Modelling and Simulation in Materials Science and Engineering 1 (3), 225–263.

Dawson, P., Boyce, D., MacEwen, S., Rogge, R., 2000. Residual strains in HY100 polycrystals: comparisons of experiment and simulations. Metallurgical and Materials Transactions A 31A (6), 1543–1555.

Dawson, P.R., Marin, E.B., 1998. Computational mechanics for metal deformation processes using polycrystal plasticity. In: van der Giessen, E., Wu, T.Y. (Eds.), Advances in Applied Mechanics, vol. 34. Academic Press, New York, pp. 78–169.

Daymond, M.R., Hartig, C., Mecking, H., 2005. Interphase and intergranular stress generation in composites exhibiting plasticity in both phases. Acta Materialia 53 (9), 2805–2813.

Efstathiou, C., Sehitoglu, H., Carroll, J., Lambros, J., Maier, H.J., 2008. Full-field strain evolution during intermartensitic transformations in single-crystal NiFeGa. Acta Materialia 56 (15), 3791–3799.

Franciosi, P., Berbenni, S., 2007. Heterogeneous crystal and poly-crystal plasticity modeling from a transformation field analysis with a regularized Schmid law. Journal of the Mechanics and Physics of Solids 55 (11), 2265–2299.

Graff, S., Brocks, W., Steglich, D., 2007. Yielding of magnesium: from single crystal to polycrystal aggregates. International Journal of Plasticity 23 (12), 1957–1978.

Hartig, C., Mecking, H., 2005. Finite element modelling of two phase Fe–Cu polycrystals. Computational Materials Science 32 (3–4), 370–377.

Holden, T.M., Clarke, A.P., Holt, R.A., 1997. Neutron diffraction measurements of intergranular strains in monel-400. Metallurgical and Materials Transactions A 28 (12), 2565–2576.

Holmedal, B., Houtte, P.V., An, Y., 2008. A crystal plasticity model for strain-path changes in metals. International Journal of Plasticity 24 (8), 1360–1379.

Honeycombe, R.W.K., 1984. The Plastic Deformation of Metals, second ed Edward Arnold.

Hosford, W.F., 1993. The Mechanics of Crystals and Textured Polycrystals. Oxford University Press, New York.

Kalidindi, S.R., Bronkhorst, C.A., Anand, L., 1992. Crystallographic texture evolution in bulk deformation processing of fcc metals. Journal of the Mechanics and Physics of Solids 40 (3), 537–579.

Klepaczko, J.R., Chiem, C.Y., 1986. On rate sensitivity of f.c.c. metals, instantaneous rate sensitivity and rate sensitivity of strain hardening. Journal of the Mechanics and Physics of Solids 34 (1), 29–54.

Knockaert, R., Chastel, Y., Massoni, E., 2000. Rate-independent crystalline and polycrystalline plasticity, application to FCC materials. International Journal of Plasticity 16 (2), 179–198.

Kocks, U.F., 1960. Polyslip in single crystals. Acta Metallurgica 8 (6), 345–352.

Kocks, U.F., 1970. The relation between polycrystal deformation and single crystal deformation. Metallurgical Transactions 1 (5), 1121–1143.

Kocks, U.F., Canova, G.R., Jonas, J.J., 1983. Yield vectors in f.c.c. crystals. Acta Metallurgica 31 (8), 1243–1252.

Kocks, U.F., Tomé, C.N., Wenk, H.R., 1998. Texture and Anisotropy. Cambridge University Press, Cambridge.

Kumar, A., Dawson, P.R., 2000. Computations modeling of f.c.c. deformation textures over Rodrigues' space. Acta Materialia 48 (10), 2719–2736.

Kumar, A., Dawson, P.R., 2009. Dynamics of texture evolution in face-centered cubic polycrystals. Journal of the Mechanics and Physics of Solids 57 (3), 422–445.

MacEwen, S.R., Faber Jr., J., Turner, A.P.L., 1983. The use of time-of-flight neutron diffraction to study grain interaction stresses. Acta Metallurgica 31 (5), 657–676.

Maniatty, A.M., Littlewood, D.J., Lu, J., 2008. Polycrystal simulations investigating the effect of additional slip system availability in a 6063 aluminum alloy at elevated temperature. Journal of Engineering Materials and Technology 130 (2), 021019-1–021019-9.

Maniatty, A.M., Yu, J.-S., 1996. Effect of elasticity on slip system activity in face-centered cubic crystals: a numerical study. International Journal of Solids and Structures 33 (8), 1069–1082.

Marin, E.B., Dawson, P.R., 1998a. Elastoplastic finite element analyses of metal deformations using polycrystal constitutive models. Computer Methods in Applied Mechanics and Engineering 165 (1-4), 23–41.

Marin, E.B., Dawson, P.R., 1998b. On modelling the elasto-viscoplastic response of metals using polycrystal plasticity. Computer Methods in Applied Mechanics and Engineering 165 (1–4), 1–21.

Marin, T., Dawson, P.R., Gharghouri, M.A., Rogge, R.B., 2008. Diffraction measurements of elastic strains in stainless steel subjected to in situ biaxial loading. Acta Materialia 56 (16), 4183–4199.

Mathur, K.K., Dawson, P.R., 1989. On modeling the development of crystallographic texture in bulk forming processes. International Journal of Plasticity 5 (1), 67–94.

Mecking, H., Kocks, U.F., Hartig, C., 1996. Taylor factors in materials with many deformation modes. Scripta Materialia 35 (4), 465–471.

Miehe, C., Rosato, D., 2007. Fast texture updates in fcc polycrystal plasticity based on a linear active-set-estimate of the lattice spin. Journal of the Mechanics and Physics of Solids 55 (12), 2687–2716.

Miller, M., Bernier, J., Park, J.-S., Kazimirov, A., 2005. Experimental measurement of lattice strain pole figures using synchrotron X-rays. Review of Scientific Instruments 76 (11), 113903.

Miller, M.P., Park, J.-S., Dawson, P.R., Han, T.-S., 2008. Measuring and modeling distributions of stress state in deforming polycrystals. Acta Materialia 56 (15), 3927–3939.

Morawiec, A., Pospiech, J., 1989. Some information on quaternions useful in texture. Textures and Microstructures 10, 211–216.

Needleman, A., Asaro, R.J., Lemonds, J., Peirce, D., 1985. Finite element analysis of crystalline solids. Computational Methods in Applied Mechanics and Engineering 52 (1–3), 689–708.

Pang, J.W.L., Holden, T.M., Mason, T.E., 1998. In situ generation of intergranular strains in an Al7050 alloy. Acta Materialia 46 (5), 1503–1518.

Phillips, A., Sierakowski, R.L., 1965. On the concept of the yield surface. Acta Mechanica 1 (1), 29–35.

Raabe, D., Sachtleber, M., Zhao, Z., Roters, F., Zaefferer, S., 2001. Micromechanical and macromechanical effects in grain scale polycrystal plasticity experimentation and simulation. Acta Materialia 49 (17).

Ritz, H., 2008. Modeling elastic anisotropy in diffraction experiments using finite elements. Ph.D. Thesis, Cornell University.

Zhang, F., Bower, A.F., Mishra, R.K., Boyle, K.P., 2009. Numerical simulations of necking during tensile deformation of aluminum single crystals. International Journal of Plasticity 25 (1), 49–69.

Zhao, Z., Ramesh, M., Raabe, D., Cuitino, A.M., Radovitzky, R., 2008. Investigation of three-dimensional aspects of grain-scale plastic surface deformation of an aluminum aligocrystal. International Journal of Plasticity 24 (12), 2278–2297.